Micro and nanoscale characterization of complex multilayer-structured white etching layer in rails

Wu, Jun; Petrov, Roumen; Kölling, Sebastian; Godet, Stephane; Sietsma, Jilt

DOI
10.3390/met8100749

Publication date
2018

Document Version
Final published version

Published in
Metals

metals

MDPI

Article

Micro and Nanoscale Characterization of Complex Multilayer-Structured White Etching Layer in Rails

Jun Wu [1,2,*], Roumen H. Petrov [1,2], Sebastian Kölling [3], Paul Koenraad [3], Loic Malet [4], Stephane Godet [4] and Jilt Sietsma [1,2]

1 Department of Materials Science and Engineering, Delft University of Technology, Mekelweg 2, 2628 CD Delft, The Netherlands; roumen.petrov@ugent.be (R.H.P.); j.sietsma@tudelft.nl (J.S.)
2 Department of Electrical Energy, Metals, Mechanical Constructions and Systems, Ghent University, Technologiepark Zwijnaarde 913, 9052 Ghent, Belgium
3 Department of Applied Physics, Technical University of Eindhoven, Technische Universiteit Eindhoven, P.O. Box 513, 5600 MB Eindhoven, The Netherlands; sebastian.koelling@gmail.com (S.K.); p.m.koenraad@tue.nl (P.K.)
4 4MAT, Materials Engineering, Characterization, Synthesis and Recycling, Université Libre de Bruxelles, Avenue F.D. Roosevelt 50, 1050 Brussels, Belgium; loic.malet@gmail.com (L.M.); sgodet@ulb.ac.be (S.G.)
* Correspondence: jun.wu@ugent.be; Tel.: +31-152-789-280

Received: 31 August 2018; Accepted: 20 September 2018; Published: 23 September 2018

Abstract: Micro- to nano-scale characterization of the microstructures in the white etching layer (WEL), observed in a Dutch R260 Mn grade rail steel, was performed via various techniques. Retained austenite in the WEL was identified via electron backscatter diffraction (EBSD), automatic crystallographic orientation mapping in transmission electron microscopy (ACOM-TEM), and X-ray diffraction (XRD). EBSD and ACOM-TEM methods were used to quantify grains (size range: 50 nm–4 μm) in the WEL. Transmission electron microscopy (TEM) was used to identify complex heterogeneous microstructural morphologies in the WEL: Nano-twinning substructure with high dislocation density in the WEL close to the rail surface and untransformed cementite and dislocations in the WEL close to the pearlite matrix. Furthermore, atom probe tomography (APT) revealed a heterogeneous through-thickness distribution of alloying elements in the WEL. Accordingly, the WEL is considered a multi-layered martensitic microstructure. These findings are supported by the temperature calculations from the shape analysis of the manganese profile from APT measurements, related to manganese diffusion. The deformation characteristics of the WEL and the pearlite beneath the WEL are discussed based on the EBSD measurements. The role of deformation in the martensitic phase transformation for WEL formation is discussed.

Keywords: white etching layer; rails; martensite; temperature; phase transformation; plastic deformation

1. Introduction

A white etching layer (WEL) [1–8] resulting from rail/wheel contact is a common microstructural feature formed on rail surfaces and is frequently associated with rolling contact fatigue (RCF) damage. During train passages, some of the initial pearlitic microstructure in the rail surface transforms into a different structure. The new structure typically appears as a 10–20 μm (thickness) featureless layer, which appears white under the optical microscope, after etching with a nitric acid solution in ethanol. Furthermore, WEL is a common problem in rails with a pearlitic microstructure as this layer occurs: (1) with different initial microstructural components, i.e., ferrite-pearlite [8] or fully lamellar pearlite [1,5,6], and (2) at various track sites, e.g., tangential tracks or curved rails. The presence of

WEL may lead to crack initiation after brittle fracture of the WEL, owing to its high hardness (up to 1200 HV) [5]. Worldwide observations of crack initiation at WELs have been reported in metallographic studies of loaded rails in various countries including Japan [9], the Netherlands [10], Australia [11], and Great Britain [12]. Carrol et al. [13,14] determined, via laboratory twin disc tests, the influence of WEL on the RCF behavior in rails and proposed that WEL facilitates both wear and RCF processes in rails. In their subsequent numerical analysis, stress/strain concentration at the WEL was detected and was considered consistent with their experimental observations.

The origin of the microstructure comprising the WEL is typically determined by employing a combination of advanced characterization methods. Detection of tetragonal deviation from the body-centered cubic (BCC) lattice and retained austenite with (synchrotron) X-ray diffraction (XRD) is commonly taken as strong evidence of martensite in the WEL [3,15]. Additional evidence includes a martensite twinning substructure observed by means of transmission electron microscopy (TEM) [3]. Using TEM, Takahashi et al. [6] determined that the WEL has a high dislocation density and consists of grains with sizes of a few hundred nanometers, which are considerably finer than the pearlite beneath the WEL. The TEM investigation was combined with atom probe tomography (APT) analysis, for quantifying the manganese diffusion in the WEL and the authors concluded that the rail temperature increased to at least to 900 °C. Accordingly, the hypothesis that WEL formation occurs via martensitic phase transformation was proposed.

The other hypothesis is that WEL consists of nanocrystalline ferrite grains, owing to strain accumulated from passing train wheels. The original pearlite/ferrite structure undergoes significant refinement to a grain sizes with sizes of tens of nanometers, and the cementite dissolves in this structure due to the plastic deformation. The extremely high hardness [7,16] is considered abnormal for a martensitic microstructure produced by standard heat treatments, but can be attributed to strengthening from the ultra-fine ferrite grains. In some cases, WEL formation is attributed to this hypothesis despite the occurrence of martensitic-like characteristics. For example, in a TEM-based investigation, Baumann et al. [2] reported a fully martensitic microstructure and a WEL without retained austenite. The corresponding calculated temperature differed significantly from the temperature required for pearlite to austenite transformation. Consequently, they attributed the WEL formation to repeated deformation.

Formation of WELs, in accordance with the aforementioned hypotheses, are strongly supported by separate laboratory simulations. For example, (ultra)fast heat treatments can produce martensite with hardness and grain sizes comparable to those of the studied WEL in rails [17], or martensite with a high hardness and a twinned substructure [3]. A similar white layer is also commonly observed in the surface of loaded components, exposed to a significant temperature increase, e.g., during surface machining [18] and hard turning [19,20]. However, nanocrystalline ferrite white layers are formed in pearlite subjected to severe plastic deformation [7,20]. The extremely high hardness of the WEL and the nanometer-sized grains that comprise it [7], can be reproduced via severe plastic deformation. Some critical strain may be required for the formation of nanometer-sized grains and complete cementite dissolution. Consequently, the microstructure in the WEL must be correlated with the loading conditions of the studied rail specimen. Regarding the wheel/rail contact, the following assumptions are considered valid: (i) WEL forms via combined plastic deformation and temperature increase and (ii) the separate contributions depend on the loading history of the rails.

However, automatic orientation mapping methods, e.g., electron backscatter diffraction (EBSD) and the recently developed automatic crystallographic orientation mapping in transmission electron microscopy (ACOM-TEM) with an improved spatial resolution [21,22], have only been employed in a few of the aforementioned studies. The EBSD and ACOM-TEM methods provide accurate crystal orientation and misorientation measurements and are inherently useful in revealing the deformation structures in the WEL [17] and the strain gradient in the rails [23,24]. Characterization and quantification of such structures by other methods, such as TEM and APT, are difficult. Moreover, EBSD can scan over a large bulk specimen, including the WEL and the surrounding matrix. Therefore,

compared with TEM and APT, EBSD provides a wider overview of differences between (e.g., the grain size, deformation scale of) the WEL and the pearlite underneath. The EBSD spatial resolution, typically 50–100 nm, may limit the identification of very fine grains in the WEL [24]. Very fine grain size (50 nm) was detected by transmission Kikuchi diffraction (TKD) in a white layer, formed after severe plastic deformation in a high carbon steel (1 mass% C) with an initial microstructure of martensite and 30–40% retained austenite [25]. Alternatively, complementary information can be provided by the ACOM-TEM method, where a spatial resolution of 2 nm has been reported for field emission TEM [21]. Therefore, EBSD and ACOM-TEM will be useful for characterizing the WEL and additional information may be extracted from the crystallographic features.

In this work, we characterize the WEL, observed in an R260 Mn grade rail, using various methods associated with different resolution levels. The formation mechanism of WEL is investigated by evaluating the crystallographic, morphological, and compositional characteristics. Techniques such as XRD, EBSD, and ACOM-TEM are used to identify the phase components of the WEL. Moreover, EBSD and ACOM-TEM are used to map the phase distribution and reveal the local misorientation changes induced by passages of the train. TEM will be used to characterize the morphological and phase constituents of the WEL at a higher resolution level than those of XRD and EBSD. The compositional variations in the WEL are revealed via APT. Finally, the WEL formation mechanism will be discussed based on the obtained results.

2. Materials and Methods

The studied WELs were taken from an R260Mn grade rail track (chemical composition: Fe-0.67 wt.% C-1.51 wt.% Mn-0.21 wt.% Si). The rail was originally implemented between 1989 and 2007 in a straight track site between Meppel and Steenwijk in the Netherlands [17]. Corrosion and oxidization products formed in the rail surface during the storage, due to unprotected laboratory storage in air after removal. These products were ground away using Struers (Struers, Westlake, OH, USA) #2000 grinding paper and the freshly revealed surface areas were etched with 2% Nital, after cleaning with ethanol. Due to the etching, part of the steel surface has a lighter color, than the gray surrounding areas (see, e.g., the photo in Figure 1a). The light color areas are located close to the two edges of the running band and are easily recognized by the naked eye. The notations RD, TD, and ND refer to directions parallel to the traffic/rolling direction (RD), transverse direction (TD), and the direction perpendicular to the rail surface (ND), respectively.

Figure 1b shows an optical micrograph of a cross-sectional specimen, cut through one of the light blocks enclosed in the white rectangle shown in Figure 1a. WEL with classic morphology (measured hardness: ~820 HV) and the pearlite underneath (hardness: 290 HV) are clearly visible. The drawing in Figure 1c shows the positions of APT-tip and TEM-lamellae extraction.

After final polishing with 1 μm diamond suspension, the light WEL zones in the rail piece shown in Figure 1a were characterized via XRD scans (Bruker Discover D8 XRD machine, Bruker AXS GmbH, Karlsruhe, Germany), parallel beam geometry, Co Kα radiation). The scanned area including WEL was approximately 11.8 × 5 mm^2, but some of the surrounding matrix regions were inevitably included in the scans, due to the non-homogeneous distribution of WELs in the rail surface. All scans were performed under the following conditions: Acceleration voltage: 45 kV, current: 25 mA, scanning step size (2θ): 0.03°, 2θ angular range: 40–95°, and scanning speed: 1 s per step. For reference, a sample cut from the rail center (i.e., a WEL-free sample) was scanned under identical conditions. Phase components of the WEL and pearlite regions were identified by comparing the 2θ positions of the diffraction peaks with the phase data in the International Center for Diffraction Data (ICDD) database [26].

After the relevant sample preparation procedure [17], the cross-sectional WEL specimen shown in Figure 1b was characterized via electron backscatter diffraction (EBSD). An FEI Quanta–450 field emission gun scanning electron microscope (FEG-SEM) (FEI, Hillsboro, OR, USA), equipped with a Hikari-Pro EBSD detector (EDAX Inc., Mahwah, NJ, USA), was used for the scans. The orientation

data were collected under the following conditions: accelerating voltage: 20 kV, FEI spot size: 5, final aperture size: 40 µm, working distance: 16 mm. The data were collected, with EDAX-TSL OIM Data Collections v6.2 software (EDAX Inc., Mahwah, NJ, USA), at a step size of 50 nm on a hexagonal grid.

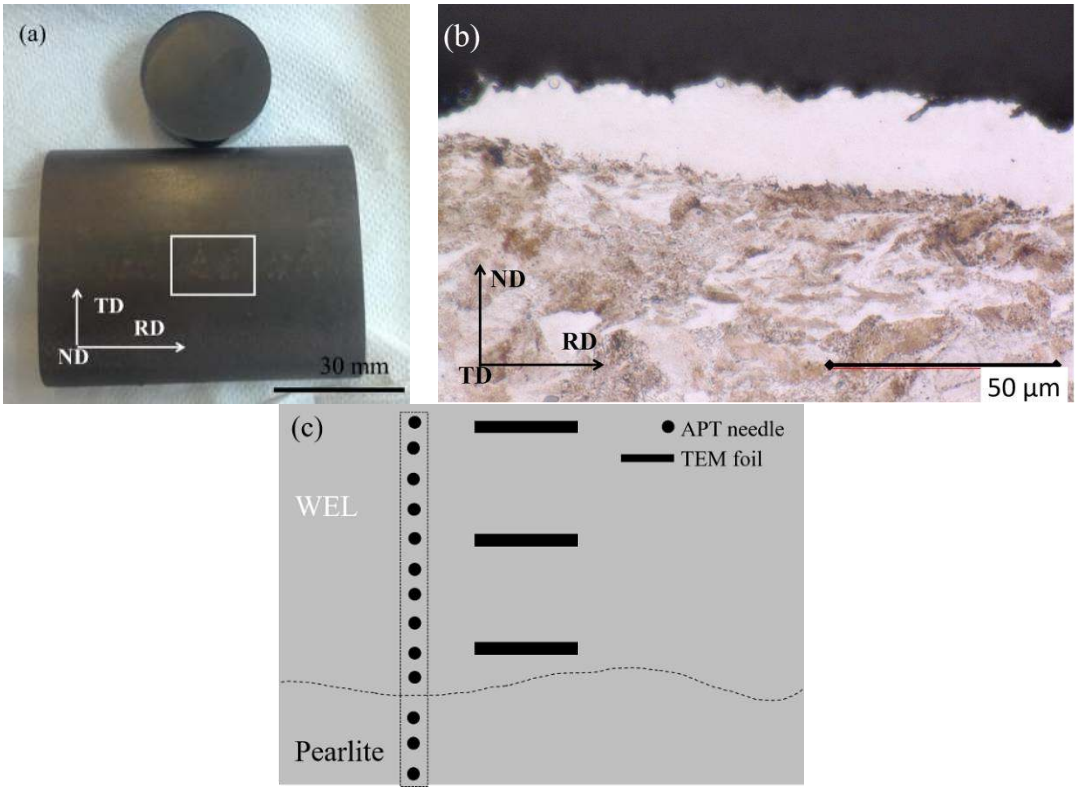

Figure 1. (**a**) An overview of the rail surface after grinding and subsequent etching with 2% Nital; (**b**) optical micrograph of a cross-sectional specimen, cut across one of the WEL blocks enclosed in the white rectangle shown in (**a**); (**c**) magnified view of the region enclosed in the white rectangle shown in (**b**), with positions of APT-pillar and TEM-lamellae extraction indicated.

Three TEM lamellae were subsequently extracted from the specimen used for EBSD scans. The lamellae were prepared via the focused ion beam milling and lift-out method using a FEI Nova 600 Nanolab DualBeam FIB-SEM (FEI, Hillsboro, OR, USA). Hereafter, the three TEM lamellae are referred to in terms of their relative original positions in the WEL, schematically shown in Figure 1c: (i) surface WEL, ~3 µm beneath the rail surface; (ii) center WEL, ~12 µm below the rail surface and approximately in the center of the WEL; (iii) interface WEL, in the WEL and ~1–2 µm above the WEL/pearlite boundary. ACOM-TEM measurements on the three lamellae were performed in a Philips CM20 TEM (FEI, Hillsboro, OR, USA), instrument, equipped with a LaB6 electron gun. The samples were scanned at an accelerating voltage of 200 keV and the data were collected using an ASTAR attachment [27]. The diffraction patterns were formed at a precession angle and camera length of 1° and 88 mm, respectively, and acquired at a rate of 70 frames per second. The TEM configuration employed for these measurements yielded an estimated probe size of 13 nm. The ACOM-TEM scan data were translated into the OSC format and were further processed as EBSD data, using version 7.30 of the OIM post-processing software.

Prior to quantification, the following cleanup procedures were applied to the EBSD and ACOM-TEM scan data: (i) grain confidence index (CI) standardization with a grain definition threshold angle of 5° and minimum grain size of 6 pixels. The orientations were maintained, but the highest CI of the defined grain was assigned to each pixel of the grain; (ii) neighbor orientation correlation. After this step, orientations of pixels with low CI, i.e., <0.1, were reassigned to the neighbor grain orientation, based on the selected parameters in the OIM software. A clean-up level of 3 was applied.

Furthermore, a minimum misorientation of 5° with the neighboring grain was defined and grains defined in EBSD and ACOM-TEM consisted of at least 10 and 40 pixels, respectively. After the cleanup procedures, the remaining pixels with CI < 0.1 were considered dubious and, hence, were removed from the EBSD scan. These points appeared as black pixels in the scans.

The same TEM lamellae were further characterized using a Jeol JEM-2200FS FEG-TEM (JEOL USA Inc., Peabody, MA, USA) with a C_s corrector for the objective lens. The experiments were performed at 200 kV, and a minimum objective aperture size of 100 nm was employed for selected area diffraction (SAD).

For compositional analysis, sharp needles along the WEL depth were prepared from the same main WEL block, as schematically shown in Figure 1c. The APT tips were extracted using a FEI Nova 600 FIB/SEM Dual Beam set-up. The APT measurements were performed via high resolution three-dimensional (HR 3D) atom probe microscopy (Cameca LEAP-4000X, CAMECA, Gennevilliers, France) in voltage mode (pulse repetition: 200 kHz, pulse fraction: 0.2, and sample temperature: 20 K). The APT data were analyzed with Imago Visualization and Analysis Software (IVAS, CAMECA, Gennevilliers, France) version 3.6.

3. Results

3.1. X-Ray Diffraction (XRD) Results

Figure 2 shows the XRD spectra obtained from scans of the surface WEL and the central reference specimen, which has a fully pearlitic microstructure [28]. The results confirm that the central reference specimen consists of cementite and ferrite. A similar phase composition is revealed by the spectrum of the surface WEL specimen, although additional {200} and {220} peaks of austenite are present. The cementite peak intensity of the surface WEL spectrum is very weak, compared with that of the reference pearlite sample. In addition, the {110} and {200} peaks of ferrite in the surface WEL specimen are broader than those of the reference sample and are slightly asymmetric. This may be attributed to peak broadening resulting from small grains or high dislocation densities. The unexpected peaks in the WEL specimen, at 42° in Figure 2, arise from the unground oxide (WEL in the rail surface is retained by avoiding excessive grinding during sample preparation for XRD measurements).

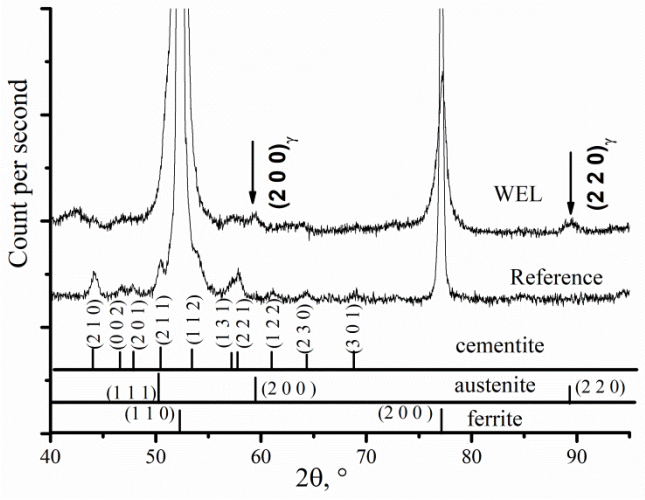

Figure 2. XRD spectra of the WEL zone at the rail surface and the reference pearlitic specimen from the rail center [28].

3.2. Electron Backscatter Diffraction (EBSD) Results

Figure 3a shows the grayscale image quality (IQ) map of ferrite, from the EBSD scan of the WEL specimen. The color-coded inverse pole figure (IPF) of austenite is superimposed on this map. No pixels were discarded for the mapping. The WEL can be differentiated from the pearlite area,

i.e., the WEL appears in dark gray shades, indicating higher dislocation density of the WEL (compared with that of the pearlite region) and/or very fine grains. The grains in the WEL are heterogeneous both in terms of size and morphology. The WEL close to the rail surface, e.g., within zone 2 of the hollow dashed rectangle in Figure 3a, exhibits random morphology. In contrast, the subsurface WEL consists of elongated grains, e.g., in zone 1 shown in Figure 3a. Furthermore, individual WELs in the pearlite zone (i.e., low-IQ regions) are observed and are partly indicated by solid black arrows in Figure 3a. Isolated WELs in the pearlite region, which are separated from the main large WEL block, are quite frequently observed and, hence, can be used to indicate the propagation characteristics of the WEL during loading.

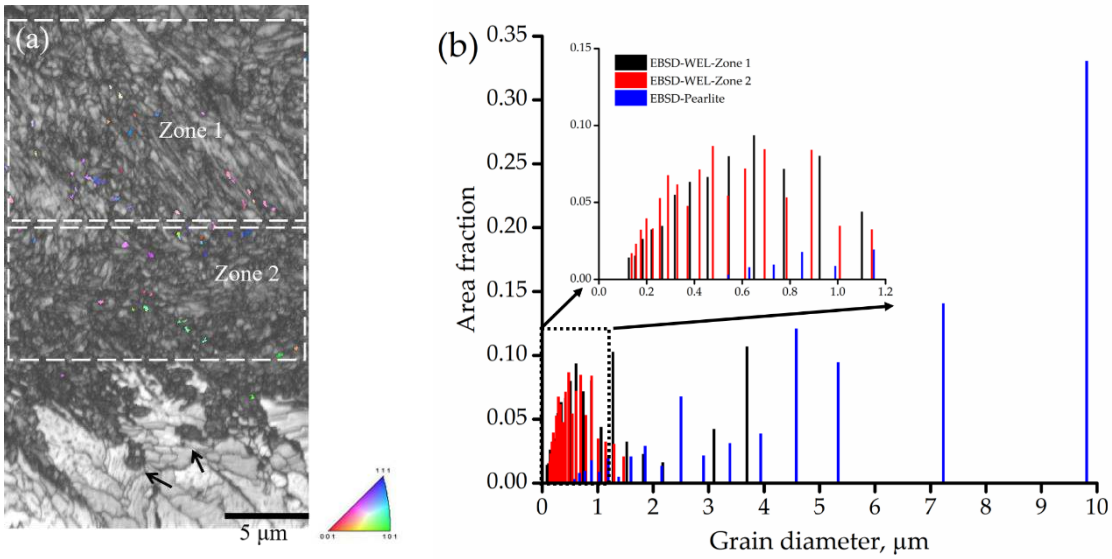

Figure 3. (**a**) The image quality map of WEL superimposed on the inverse pole figure map of austenite. Part of the pearlite beneath the WEL is also included in the mapping; (**b**) comparison of the grain diameter associated with zone 1 and zone 2 in (**a**) and the pearlite area.

Austenite occurs frequently in the WEL (see the superimposed IPF in Figure 3a). However, a clear correlation between the austenite distribution and position along the WEL depth is lacking, as austenite grains are located both close to the rail surface and close to the WEL/pearlite boundary.

Figure 3b shows the grain size distribution of the BCC phase, quantified from zone 1 and zone 2 in Figure 3a. The grain size distribution of the pearlite area beneath the WEL is included for comparison. The grain size range of zone 1 (190 nm–4 μm) is wider than that of zone 2 (180 nm–2 μm). Furthermore, the grain size of the pearlite ferrite underneath the WEL zones (i.e., 113 nm–10 μm) is larger than that of the WEL zones. The average grain size of zone 1, zone 2, and the pearlite ferrite are 388 ± 298 nm, 320 ± 174 nm, and 798 ± 320 nm, respectively. Most of the grains are sub-micrometer sized, and only a few grains have sizes >1 μm.

Figure 4a shows the kernel average misorientation (KAM) map of the BCC phase in the WEL, Figure 3a, using a threshold of 5° and 1st neighbor relations. The dark zones result from the applied threshold of 5° and 4 pixels corresponding to the grain definition. The fraction of green and yellow, misorientation of 1–3°, in the WEL indicates the deformation history of the rails. Such zones occur considerably less frequently in the pearlite region (in Figure 4a), than in the WEL, and are mainly located at the grain boundaries and the cementite/ferrite phase boundaries. Figure 4b shows a plot of the BCC KAM distribution, mapped from the entire WEL and the pearlite underneath the WEL. The KAM plot of a deformation-free reference area, 500 μm beneath the rail surface, is included for the sake of comparison. As the figure shows, the WEL is characterized by a distinctly higher KAM than the subsurface pearlite and reference pearlite, which have similar KAM distributions.

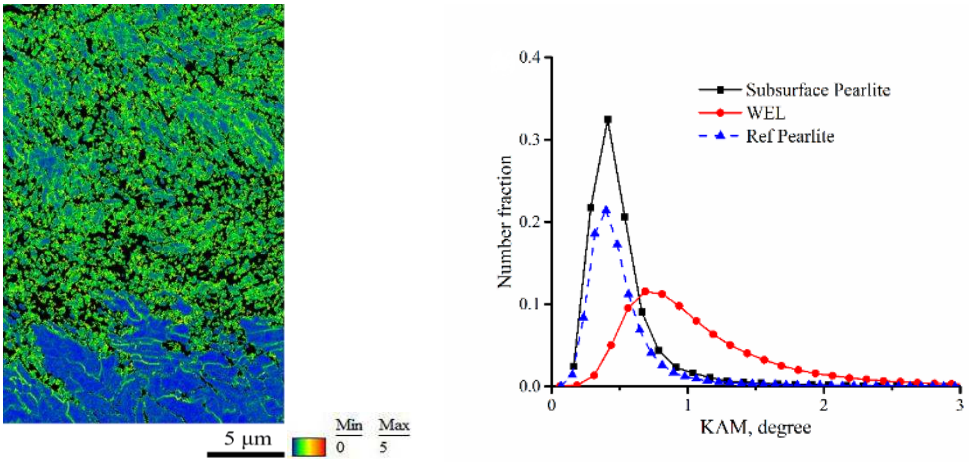

Figure 4. (**a**) KAM map of the WEL specimen, using 5° and 1st neighbor and (**b**) KAM plot of ferrite in the WEL and pearlite underneath the WEL.

3.3. Results of Automatic Crystallographic Orientation Mapping in Transmission Electron Microscopy (ACOM-TEM)

Figure 5a–c shows the ACOM-TEM virtual bright field (VBF) images, superimposed on the color-coded IPF of austenite, of the three TEM foils extracted from the WEL. The martensite-like morphology can be seen in the VBF image of the surface WEL and center WEL, Figure 5a,b. The grains in both lamellae are heterogeneous and the grains in the central WEL seem finer than those in the surface. Moreover, the microstructure in the interface WEL, see Figure 5c, differs from those in Figure 5a,b. The microstructure shown in Figure 5c is characterized by a lamellar structure, indicated by black arrows, and may be indicative of the untransformed cementite retained from the original pearlite. The white line boundaries, corresponding to an angle/axis rotation of 90°<112> show the boundary character of the austenite and the bcc matrix. The highest fraction of retained austenite is obtained for the central specimen and austenite grains are frequently observed at the recognized grain boundaries.

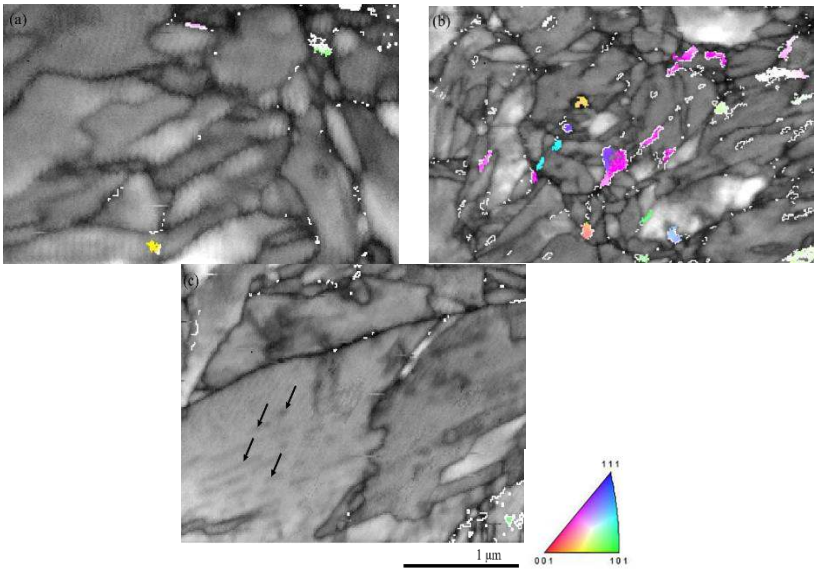

Figure 5. Virtual bright field (VBF) images superimposed on the IPF map of austenite in the (**a**) surface WEL; (**b**) central WEL; (**c**) interface WEL. Austenite grains are colored according to the IPF scheme. The black arrows indicate the possible untransformed cementite. The same scale is used for all the images.

Figure 6a shows the equivalent grain diameter distribution of the BCC phase in the surface WEL, center WEL, and interface WEL. The grain size of the surface and center WEL is comparable, and the finest grain size range (below 800 nm) occurs in the central WEL. The interface WEL is characterized by a relatively coarse grain size, i.e., >1 µm. Values of 204 ± 190 nm, 150 ± 113 nm, and 241 ± 145 nm, are obtained for the average grain size of the surface WEL, central WEL, and interface WEL, respectively. Figure 6b shows the KAM distributions of the three TEM foils, where almost identical distributions are obtained for the three zones of the WEL.

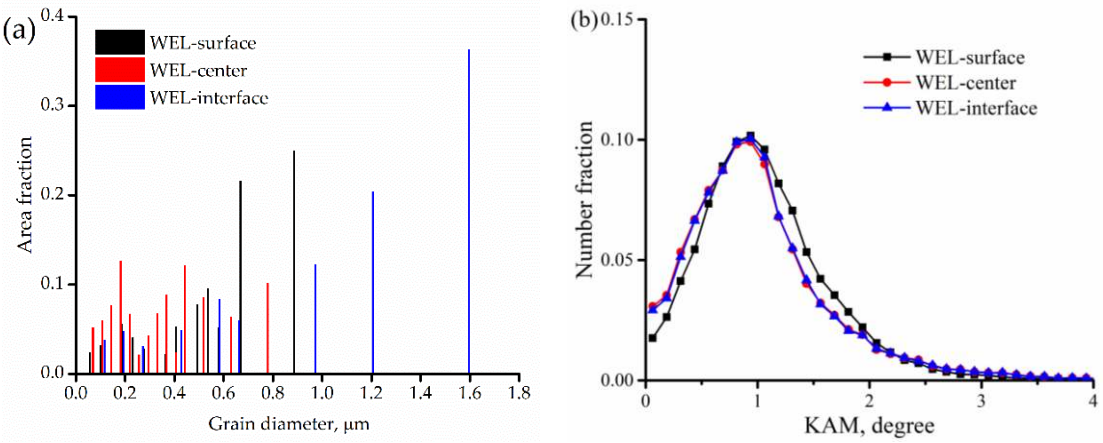

Figure 6. (**a**) Area fraction vs. grain diameter of the characterized TEM foils; (**b**) KAM plot of the characterized TEM foils, using 4th neighbor.

3.4. Transmission Electron Microscopy (TEM) Results

Figure 7a shows a representative bright field (BF) TEM image of the surface WEL specimen. The high dislocation density and the twinning-like structures occur throughout the TEM foil. Figure 7b shows the selected area diffraction (SAD) pattern of the area enclosed in the yellow circle in Figure 7a. The indexing identifies a {112} type twinning (the simulated pattern of Figure 7b is shown in Figure 7d), and the black arrow indicates the {112} twinning planes. Figure 7c shows a dark field (DF) image, obtained from the $(\bar{2}11)$ reflection of the twinning plane. Due to the high dislocation density in the characterized TEM foil, an accurate quantification of the dislocation density is impossible.

Figure 8 shows a typical BF image of the center WEL TEM foil. This specimen consists of pronounced twinned structures and high dislocation density regions, which are less common in the sub-surface WEL zone than in the surface WEL.

Figures 9a–d and 10a–d show two examples of the microstructures comprising the interface WEL. The twinning structure in this specimen is less pronounced than the structure in the surface and sub-surface WEL. A lamellar morphology, with fragmented (apparently) parallel lamellae, is observed in the BF image shown in Figure 9a. Figure 9b,d shows a SAD pattern and corresponding indexed pattern, respectively, of the region enclosed in the yellow circle shown in Figure 9a. The indexed pattern reveals the following orientation relationship:

$$(112)_{\alpha} // (\bar{2}\bar{3}3)_{\theta} \quad (1)$$

$$[\bar{6}\bar{4}1]_{\alpha} // (\bar{6}95)_{\theta} \quad (2)$$

This orientation relationship concurs with the Bagaryatsky orientation relationship between cementite (θ) and ferrite (α) [29] and, hence, the dark elongated structures are probably retained or partially dissolved cementite.

The dark field (DF) image in Figure 9c is obtained from the $(2\bar{1}1)_{\theta}$ reflection.

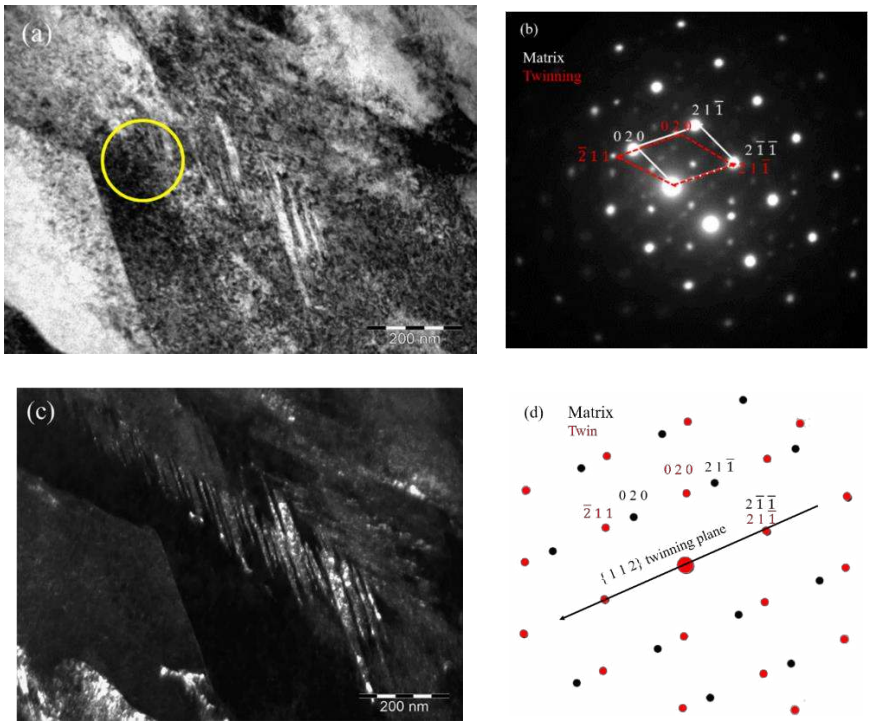

Figure 7. (**a**) A BF image of the WEL surface in the TEM foil; (**b**) Selected area diffraction (SAD) pattern, corresponding to zone axis [102]matrix of the region enclosed in the yellow circle; The (**c**) DF image formed from the $(\bar{2}11)$ reflection of the twinning plane and (**d**) simulated diffraction pattern corresponding to (**b**).

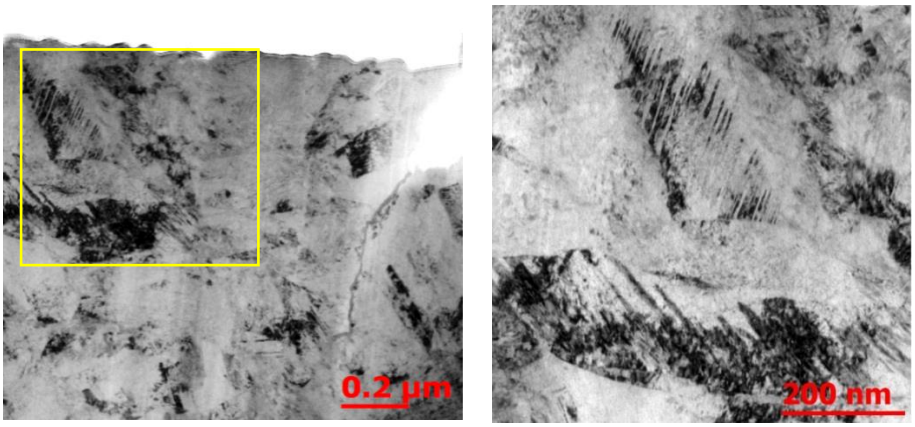

(**a**) (**b**)

Figure 8. A (**a**) representative BF micrograph of the microstructure comprising the central WEL and (**b**) magnified view of the rectangle in (**a**).

The images in Figure 10a–d show another example of the microstructure comprising the interface WEL TEM foil, where the lamellar structure (see Figure 9a) is missing. The indexing of the SAD pattern in Figure 10b reveals the orientation relationship:

$$(0\bar{1}1)_{\alpha} // (022)_{\theta} \quad (3)$$

$$[100]_{\alpha} // (0\bar{1}1)_{\theta} \quad (4)$$

The DF image in Figure 10c is obtained from the $(211)_{\theta}$ reflection. Figures 9a and 10a reveal the high dislocation density of the material.

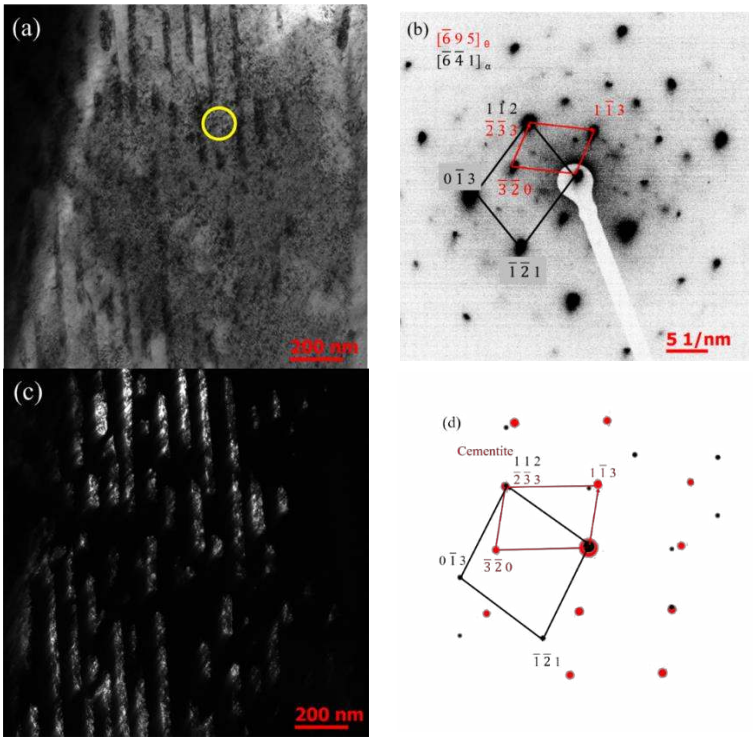

Figure 9. The (**a**) BF image of the interface WEL-TEM specimen; (**b**) SAD pattern and (**d**) indexed pattern of the region enclosed in the circle shown in (**a**). The DF image in (**c**) is obtained from the $(2\bar{1}1)$ reflection of cementite.

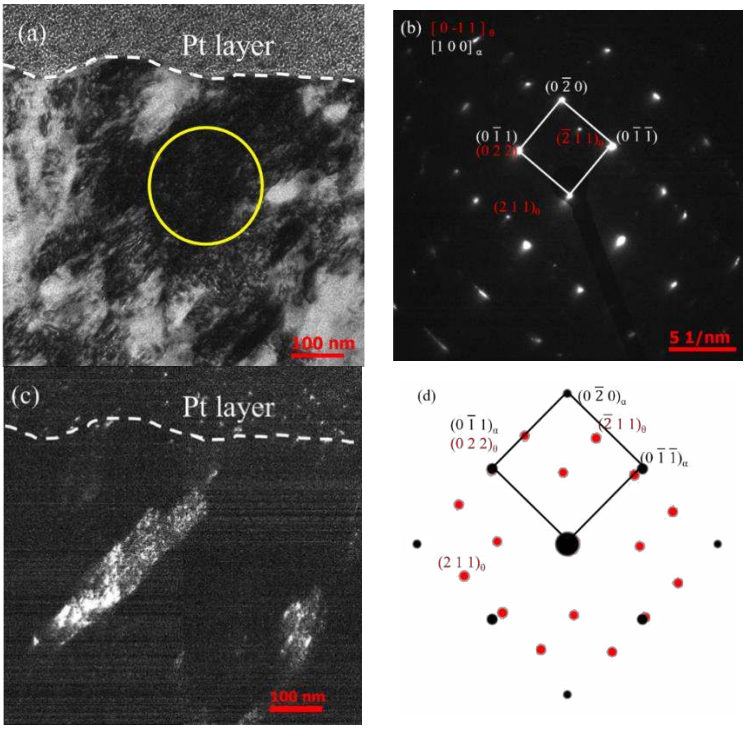

Figure 10. The (**a**) BF image of another area in the WEL-interface TEM specimen; (**b**,**d**) SAD pattern and indexed pattern, respectively, of the region enclosed in the circle shown in (**a**). The DF image in (**c**) is obtained from the (211) reflection of cementite.

3.5. Atom Probe Tomography (APT) Results

Figure 11a shows the atomic distribution of carbon, manganese, and silicon in an APT needle, extracted ~28 μm beneath the rail surface and ~3 μm beneath the WEL. A carbon- and manganese-rich silicon-depleted particle is observed. The quantification of the atomic concentration in an area across the particle is shown in Figure 11b. The carbon concentration of the area (i.e., 25 at%) indicates that this is a cementite particle. The cementite is rich in manganese. The manganese content, ~6.7 at%, is close to the equilibrium concentration at low temperature, e.g., 200 °C, as determined from Thermo-Calc. Furthermore, the silicon concentration of the silicon-rich ferrite, is comparable to the equilibrium concentration of the pearlitic ferrite.

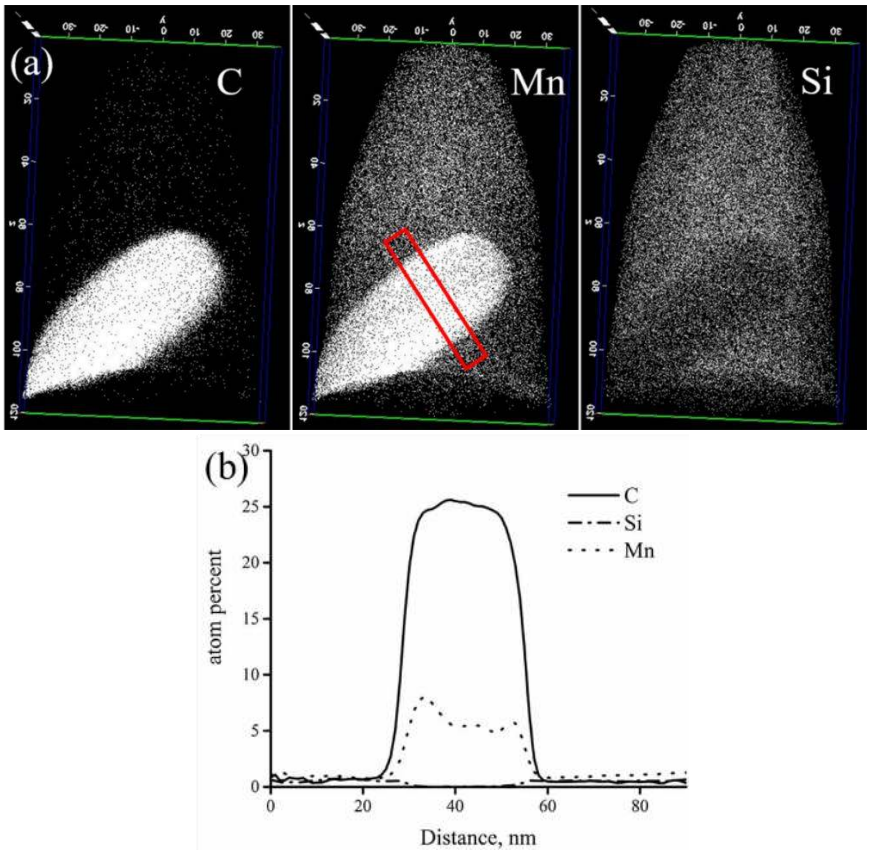

Figure 11. The 3D element maps of the APT needle taken from pearlite ~3 μm beneath the WEL (**a**) and the composition profile of regions enclosed in the rectangle in (**a**) is shown in (**b**).

Figure 12 shows the analysis results of an APT needle extracted at ~2 μm beneath the rail surface, equivalent to the surface WEL. Manganese and silicon are homogeneously distributed, whereas carbon is segregated. The segregation site and matrix are characterized by carbon content of ~9.5 at% and ~2 at%, respectively.

Figure 13 shows the analysis results of an APT needle extracted from ~10 μm beneath the rail surface, equivalent to the central WEL. The manganese-rich and silicon-poor zones indicate locations of prior cementite. However, the manganese-rich zone is characterized by weak carbon segregation and the carbon distribution throughout the APT tip seems more homogeneous than the manganese and silicon distribution. The composition profiles in the manganese-rich zones reveal a carbon concentration of ~5 at%. This concentration is higher than the average 3 at% (0.67 wt.%) determined for the overall carbon concentration of the studied R260 Mn grade rail steel, but is significantly lower than the 25 at% determined for the cementite. The composition profile of a region without the manganese-rich zone, shown in Figure 13c, reveals a carbon concentration spike of 10 at%.

Both quantifications indicate that carbon enrichment occurs in areas corresponding to and lying outside the original cementite locations.

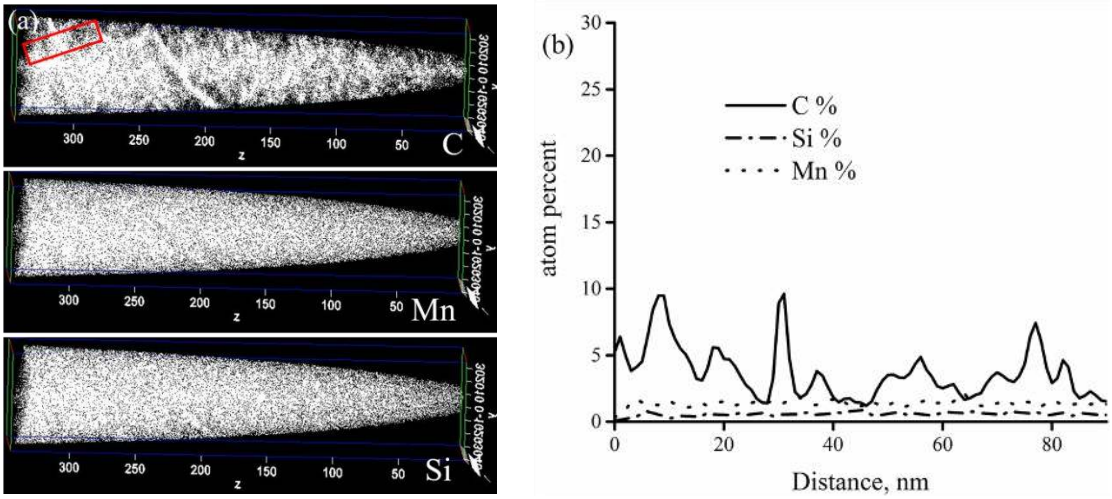

Figure 12. The 3D element maps of an APT needle taken in WEL, ~2 μm beneath the rail surface (**a**) and the composition profiles of regions enclosed in the rectangle in (**a**) is shown in (**b**).

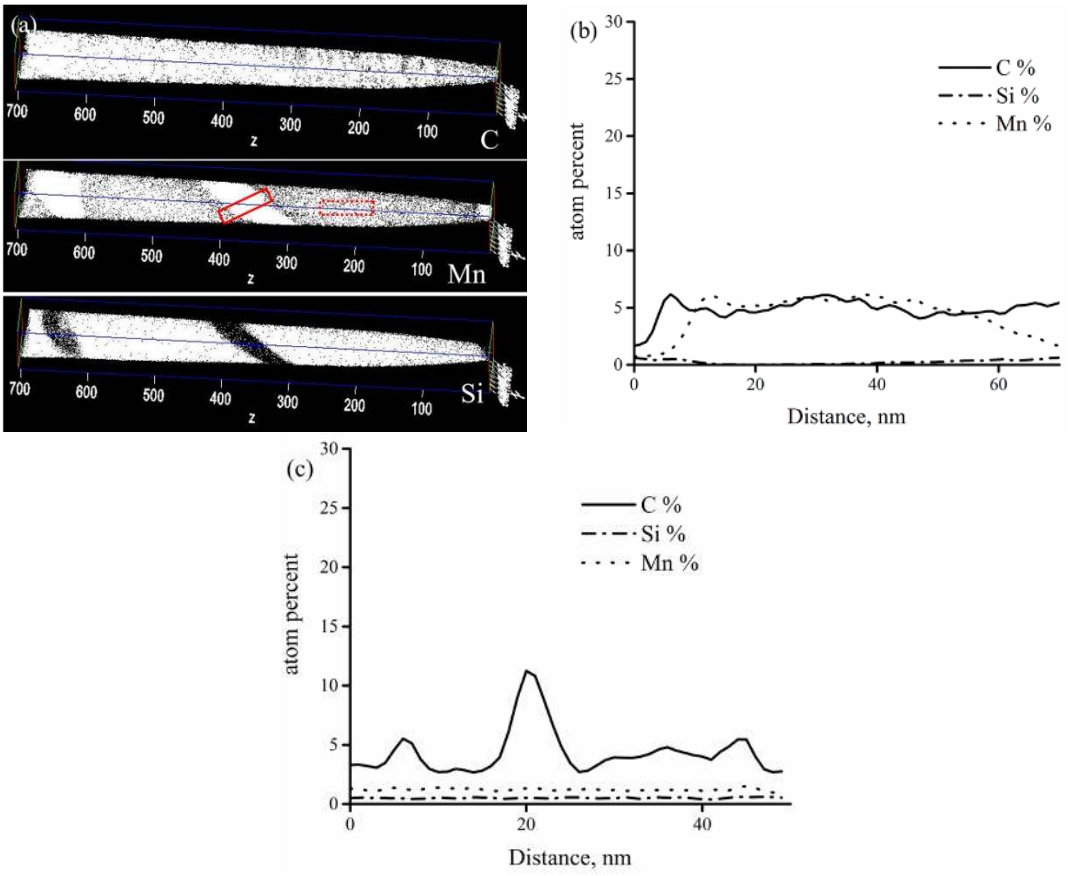

Figure 13. The 3D element maps of an APT needle taken in WEL, ~10 μm the beneath rail surface (**a**) and the composition profiles of regions enclosed in the solid rectangle and the dotted rectangle in (**a**) are shown in (**b**,**c**), respectively.

Figure 14 shows the carbon, manganese, and silicon profiles of a needle in the WEL near the WEL/pearlite boundary, equivalent to the interface WEL. A lamella, enriched in carbon and manganese

and depleted in silicon, is identified. The region enclosed within the red rectangle (see Figure 14a) is evaluated. The results reveal a carbon concentration of 25 at% for cementite (see Figure 14b), and that the cementite border is more diffuse than the cementite in the matrix (see Figure 11b).

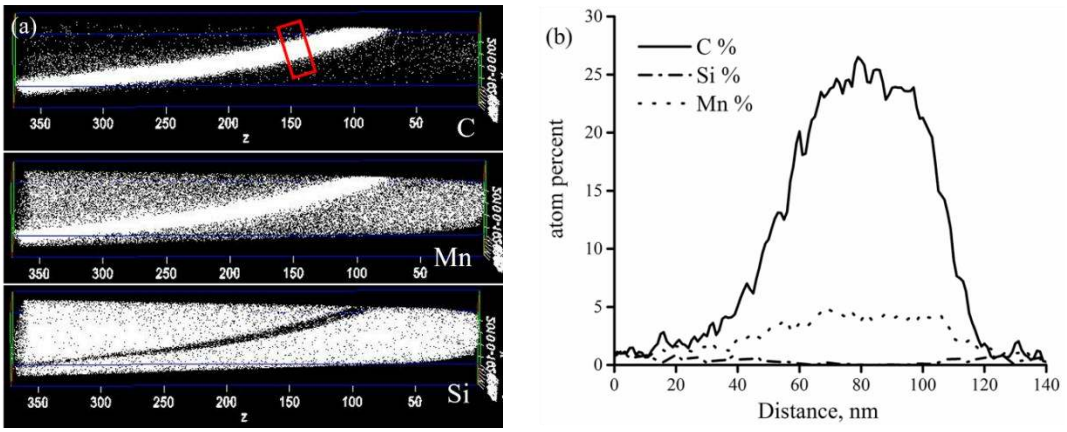

Figure 14. The 3D element maps of an APT needle taken in the WEL and close to the WEL/pearlite boundary (**a**) and the composition profiles of volumes enclosed in the hollow rectangle (**b**).

4. Discussion

4.1. The Complex Microstructure of the WEL

The applied methods consistently identify the characterized WEL as a martensitic microstructure. Evidence of this microstructure is provided by the common detection of retained austenite via XRD (Figure 2), EBSD (Figure 3a), and ACOM-TEM (Figure 5a–c) [3]. The slightly asymmetric profiles at $\{200\}_\alpha$ and $\{110\}_\alpha$ peaks in Figure 2 indicate minor lattice tetragonality, expected from martensite with an average carbon content of ~0.67 wt.%. Furthermore, the identified nano-twinning in the WEL, Figures 7a–b and 8, is expected in martensite. This morphology was observed for martensite produced through heat treatment (e.g., by laser treatment [3,17]) of rail steels with a similar composition to the steel considered in this study. Moreover, the redistribution of manganese is an important indicator of a high temperature increase, possibly up to 1400 °C, in rails [6]. In the present study, the temperature is calculated from the manganese profile using the procedure described in reference [6].

The martensite in WEL is characterized by a heterogeneous morphology and complex compositional characteristics along the rail depth, as revealed by TEM and APT. The martensite in the topmost surface WEL lamellae consists of nano-twinned substructures with a very high dislocation density, Figure 8a. No cementite is identified during indexing of the selected area diffraction pattern. The manganese and silicon profiles of the APT needles from this region, Figure 12, are homogeneous, whereas the carbon profile reveals nano-segregation, with a maximum C content of 9 at%. These profiles differ significantly from those of the pearlite regions underneath the WEL (see Figure 11), which indicate redistribution of manganese and silicon during wheel passages. Carbon spikes of up to 9.5 at% are shown in Figure 12 and are frequently identified in other regions of the same APT needle. Accommodation of this high carbon concentration by dislocations only is difficult, but accommodation by grain boundaries, twins [30,31], and retained austenite [31]. The typical distance between the carbon spikes (i.e., 5–30 nm) is considerably smaller than the martensite grain size measured via ACOM-TEM, Figure 7a, or EBSD, Figure 3b. In addition, retained austenite may also accommodate carbon, but the low austenite fraction, i.e., $\leq$6%, cannot explain the frequent observations of these spikes. Consequently, the accommodation of the most significant carbon spikes is attributed to martensite twins.

The martensite morphology (i.e., with nanotwinning and dislocations) in the center of the WEL, Figure 8, is similar to that of the surface WEL (see Figure 7), although the compositional

profile is different. The manganese-rich and silicon-poor zones remain observable in the APT needle, Figure 13, while the carbon concentration at identical zones is considerably lower than the equilibrium 25 at% for cementite. Therefore, these zones probably correspond to the original cementite sites. Furthermore, the lack of a clear correlation between the carbon spikes and the manganese-rich zones, e.g., Figure 13b,c, is indicative of carbon redistribution in the WEL. The microstructural morphology in the bottom of WEL differs completely from the morphology of the center and surface WEL. Untransformed cementite, which appears fragmented, is detected by both electron diffraction and APT. This probably corresponds to the lamellar traces observed in the ACOM-TEM map obtained at a similar depth (Figure 5c), where cementite was excluded from the phase list for indexation with ACOM-TEM and is, hence, unidentified.

The characterized WEL differs from those reported in [5,6], where the WEL was investigated through a combination of APT and TEM, as in the case of this study. The differences may be summarized as follows: the nano-twinning substructure identified in this work, e.g., Figure 7, is not reported in references. [5,6], and the grain structure is different. Zhang et al. [5] identified nano-sized grains in the top part of the WEL, using a ring diffraction pattern and a dark field TEM image. Fragmented cementite in the bottom of the WEL was detected via electron diffraction. Such fragmented cementite is also observed in the bottom of the investigated WEL, Figure 9a–d. However, nano-sized grains are absent from the topmost WEL (see Figure 7a,b), as evidenced by the lack of a ring pattern. Referring to the hypothesis proposed in this study, i.e., WEL formation is induced by phase transformation, the fragmented cementite may have resulted from heterogeneous nucleation and growth of austenite at the ferrite/cementite phase boundaries.

The APT analysis of WEL (see Figures 12–15) yields similar results to the observations reported in reference [6]. Takahashi et al. [6] identified zones with a homogeneous manganese distribution and carbon-enriched zones without manganese clustering in a WEL, and concluded that these zones were martensite formed via phase transformation. Such observations concur with the current APT results (Figures 12 and 13). The conclusion regarding the WEL is reinforced by additional observations of the martensite morphology as well as TEM, EBSD, and ACOM-TEM detection of austenite in the WEL. Cementite lamellae are absent from WEL shown in the TEM images in [6], but are observed in the current study (Figures 9 and 10). Zhang et al. [5] detected a heterogeneous carbon distribution in an APT tip, without showing the profile of manganese. Correlating the carbon clusters with the sites of the original cementite is therefore impossible. In other words, the microstructural morphology and the compositional characteristics of the characterized WEL are different from those of WELs reported in the literature.

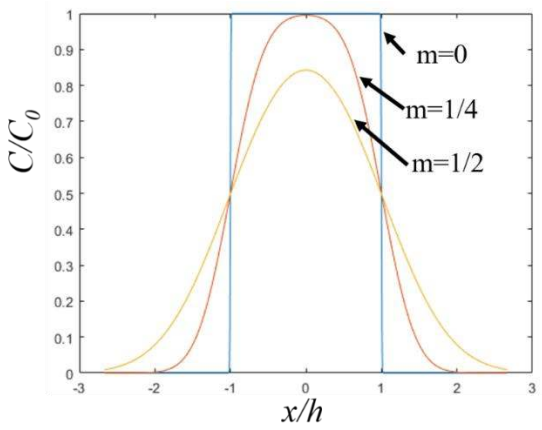

Figure 15. Schematic showing the shape analysis of manganese profiles. C and C_0 represent the manganese concentrations in the WEL and pearlite cementite, respectively; x/h is the ratio of the manganese diffusion distance to the original cementite width; m represents the ratio of the diffusion length to the zone width (additional details are provided in the main text).

Characterization, via EBSD, offers additional insight into the formation of the studied WEL. This technique enables a larger overview (i.e., larger samples and, hence, larger areas can be scanned) of the WEL than, for example, TEM. Scans revealed coarse grains, with sizes of up to 4 µm, in the WEL. Complimentary to the EBSD scans, ACOM-TEM measurements can also be used to quantify micrometer-sized grains. These grain sizes are significantly larger than those measured in TEM- [5,6] or XRD-based [7] studies, where grain sizes of ~700 nm are barely encountered. In addition, the KAM profile measured in the matrix beneath the WEL is comparable to that of the pearlite in an undeformed region. This indicates negligible deformation in the zones and is consistent with the absence of a transient work-hardened zone below the WEL, as shown by the hardness measurement in reference [17]. Therefore, the EBSD and ACOM-TEM analyses support the hypothesis of WEL formation via martensite phase transformation.

4.2. Temperature Estimation via Shape Analysis

The temperature changes in the studied rails can be estimated by analyzing the shape of the manganese profile corresponding to the WEL, e.g., [6]. Manganese diffusion can be described by Fick's law, using error functions:

$$\frac{C}{C_0} = 0.5\left\{\operatorname{erf}\left\{\frac{1-\frac{x}{h}}{\frac{2\sqrt{Dt}}{h}}\right\} + \operatorname{erf}\left\{\frac{1+\frac{x}{h}}{\frac{2\sqrt{Dt}}{h}}\right\}\right\} \quad (5)$$

where, C and C_0 are the manganese concentration after diffusion and in the initial stage respectively. Similarly, x, D, t, and h are the distance, diffusion coefficient of manganese in austenite, diffusion time, and thickness of the cementite lamella, respectively.

Owing to the elevated temperature and the contact time, the original steep manganese profile of the pearlite can become diffuse due to Mn diffusion in austenite. The Mn diffusivity depends on the temperature and the time allowed for diffusion. The schematic in Figure 15 shows the diffusion-induced changes in the manganese profile (initial composition: C_0, initial width: $2h$), with the variable m for each line corresponding to $\frac{2\sqrt{Dt}}{h}$. The estimated manganese concentrations of the APT tips are shown in Table 1. The reference manganese peak concentration, used for calculating the manganese diffusion distance, is chosen from the measured cementite only. The manganese concentration in cementite can differ among lamellae due to different forming conditions and the manganese diffusion distance in the WEL, and the temperature required for the diffusion distance is thereby affected. An m of ~0.5, corresponding to a maximum temperature of ~1400 °C, is obtained for the surface WEL.

Table 1. Manganese concentration of needles at different depths in the WEL and in the pearlite matrix.

Region	Position, µm	Mn Peak Concentration, at%	Shape	Estimated t (°C)
Surface WEL	5	4.10	Diffuse	~1400
Interface WEL	23	5.32	Slightly diffuse	<1150
Pearlite	26	5.44	Non-diffuse	-

4.3. Formation Mechanism of the Multi-Layered Structure Characterizing Martensite in the WEL

Train-passage-induced simultaneous deformation and frictional heat on the rails are expected. The deformation is indicated by the high KAM (resulting possibly from localized crystal lattice distortion) revealed by the EBSD scan of the WEL. The KAM profile of the pearlite immediately beneath the WEL indicates negligible deformation in this zone. Furthermore, the abrupt change in the KAM profile from the WEL to the pearlite underneath indicates that the thermally-induced martensitic transformation is the dominant contributor to WEL formation considered in this study.

In situ observation of the exact WEL formation mechanism is impossible, due to practical limitations associated with the complex loading conditions of the wheel/rail contact. However,

the principal formation mechanism of the multi-layered structure martensite in the studied WEL, e.g., Figures 7–10 and Figures 12–14, can be interpreted on the basis of phase transformation theory. The identified morphological and compositional characteristics of martensite in the APT tips and TEM lamellae, extracted at different depths in the WEL, are attributed to variations in the thermal history at the corresponding positions.

According to the hypothesis attributing WEL formation to martensitic phase transformation, the initial pearlitic microstructure in the rails transforms to austenite when the rail surface is heated to very high temperatures (i.e., austenitized) by the train wheels. The austenite subsequently transforms to martensite due to the rapid cooling after the train passes. On the one hand, the chemical composition and microstructures of the product martensite depend on the composition of the parent austenite [32]. On the other hand, the austenite composition depends on the characteristics of the pearlite to austenite transformation. An understanding of the pearlite to austenite transformation process is therefore essential for interpreting the multi-layered structures of the martensite in the characterized WEL.

The final characteristics of the WEL are imparted during multiple wheel passages. In this process, the pearlite to austenite transformation is followed by martensite formation during cooling. The martensite serves as the initial microstructure for the subsequent phase transformation cycles. In the literature, the reverse martensite to austenite transformation is widely considered a compositional invariant, i.e., the parent and product phases have the same composition.

The pearlite to austenite transformation is considered a diffusional process [33], characterized by the redistribution of carbon between the initial phases and austenite. Moreover, manganese partitioning between ferrite/cementite and austenite, albeit on a very fine scale that is observable via high-resolution characterization only, is typical of this transformation. These diffusional processes are temperature- and time-dependent and the ferrite and cementite to austenite transformation may be incomplete if carbon diffusion in austenite is limited, e.g., due to the limited diffusion time during fast heating and the use of temperatures residing in the lower range of the austenite phase region [17,33].

Simulations show that the most favorable conditions for the pearlite to austenite transformation occur at the rail surface, where the temperature is highest [17]. The temperature decreases rapidly from the surface to the rail center. As a result, compared with the region closer to the rail center, the surface region experiences higher temperatures and longer dwelling times within the austenite temperature range. This implies that the diffusion distances are longer and consequently carbon and manganese are more homogeneously distributed in the surface than in the center. The compositional characteristics of the APT tip from the bulk pearlite (see Figure 11) are compared with those of the tips from different depths in the WEL. A clear tendency for manganese and carbon segregation with increasing depth in the WEL is revealed. The absence of the 25 at% carbon zone from the rail-surface tip (see Figure 12) and the WEL-center tip (see Figure 13) indicates the full dissolution of cementite. Therefore, an overall steel carbon concentration of 0.67 wt.% is assumed for the austenite. Martensite with this carbon concentration is expected to have a twinning substructure with high dislocation density, similar to those observed for the surface WEL and the center WEL (Figures 7 and 8). However, due to the local conditions, less diffusion occurs at the bottom of WEL (than at the top). Therefore, the pearlite is only partly transformed to austenite and cementite persists, as revealed via TEM (Figures 9 and 10) and APT (Figure 14).

5. Conclusions

The WEL in an R260 Mn grade rail steel was characterized via XRD, EBSD, ACOM-TEM, TEM, and APT. The retained austenite identified via XRD, EBSD, and ACOM-TEM and the martensitic microstructure revealed by means of TEM indicate that the WEL forms via martensitic phase transformation. A complex multi-layer structure in the WEL is revealed by TEM and APT. The microstructure comprising the WEL close to the rail surface consists of nano-twinned martensite with a high dislocation density. The bottom side of the WEL (with a high dislocation density) consists of ferrite and untransformed cementite. The manganese diffusion revealed via APT analysis provides

strong evidence for the significant temperature increase, which leads to WEL formation. The observed microstructure is consistent with the suggested phase transformation mechanisms.

The results confirm that EBSD and ACOM-TEM are useful complementary tools for characterizing and tracing the origin of WEL. These techniques reveal a WEL grain size of 50 nm–4 μm and the hypothesis of WEL formation via severe plastic deformation only is thereby excluded. The KAM measurement has been widely used to investigate the local misorientation induced by plastic deformation. This measure reveals differences in deformation length scales characterizing the WEL and the matrix pearlite. The comparison of KAM in the WEL and the pearlite immediately beneath the WEL indicates that deformation plays a secondary role in WEL formation.

Author Contributions: Conceptualization, R.H.P. and J.S.; software and methodology, L.M., S.G., P.K., and S.K.; validation, J.W., R.H.P., and J.S.; formal analysis, J.W.; writing—original draft preparation, J.W.; writing—review and editing, J.W.; supervision, R.H.P. and J.S.; project administration, J.S.

Funding: This work is financially supported by STW-the Dutch Technology Foundations and ProRail, in the framework of the project PRIME (High Performance Rail through Intelligent Metallurgy & Engineering), grant number 12247.

Acknowledgments: ProRail is acknowledged for supporting the research by providing the material and data for the study.

Conflicts of Interest: The authors declare no conflict of interest.

References

1. Dikshit, V.; Clayton, P.; Christensen, D. Investigation of rolling contact fatigue in a head-hardened rail. *Wear* **1991**, *144*, 89–102. [CrossRef]
2. Baumann, G.; Fecht, H.J.; Liebelt, S. Formation of white-etching layers on rail treads. *Wear* **1996**, *191*, 133–140. [CrossRef]
3. Österle Rooch, H.; Pyzalla, A.; Wang, L.W.; OeSterle, W.; Rooch, H.; Pyzalla, A.; Wang, L.; Österle, W.; Rooch, H.; Pyzalla, A.; et al. Investigation of white etching layers on rails by optical microscopy, electron microscopy, X-ray and synchrotron X-ray diffraction. *Mater. Sci. Eng. A* **2001**, *303*, 150–157. [CrossRef]
4. Wild Wang, L.; Hasse, B.; Wroblewski, T.; Goerigk, G.; Pyzalla, A.E. Microstructure alterations at the surface of a heavily corrugated rail with strong ripple formation. *Wear* **2003**, *254*, 876–883. [CrossRef]
5. Zhang, H.W.; Ohsaki, S.; Mitao, S.; Ohnuma, M.; Hono, K. Microstructural investigation of white etching layer on pearlite steel rail. *Mater. Sci. Eng. A* **2006**, *421*, 191–199. [CrossRef]
6. Takahashi, J.; Kawakami, K.; Ueda, M. Atom probe tomography analysis of the white etching layer in a rail track surface. *Acta Mater.* **2010**, *58*, 3602–3612. [CrossRef]
7. Lojkowski, W.; Djahanbakhsh, M.; Bürkle, G.; Gierlotka, S.; Zielinski, W.; Fecht, H.J. Nanostructure formation on the surface of railway tracks. *Mater. Sci. Eng. A* **2001**, *303*, 197–208. [CrossRef]
8. Newcomb, S.B.; Stobbs, W.M. A transmission electron microscopy study of the white-etching layer on a rail head. *Mater. Sci. Eng.* **1984**, *66*, 195–204. [CrossRef]
9. Ishida, M. Rolling contact fatigue (RCF) defects of rails in Japanese railways and its mitigation strategies. *Electron. J. Struct. Eng.* **2013**, *13*, 67–74.
10. Steenbergen, M.; Dollevoet, R. On the mechanism of squat formation on train rails–Part I: Origination. *Int. J. Fatigue* **2013**, *47*, 361–372. [CrossRef]
11. Pal, S.; Valente, C.; Daniel, W.; Farjoo, M. Metallurgical and physical understanding of rail squat initiation and propagation. *Wear* **2012**, *284–285*, 30–42. [CrossRef]
12. Clayton, P. Tribological aspects of wheel-rail contact: A review of recent experimental research. *Wear* **1995**, *191*, 170–183. [CrossRef]
13. Carroll, R.I.; Beynon, J.H. Rolling contact fatigue of white etching layer: Part 1. Crack morphology. *Wear* **2007**, *262*, 1253–1266. [CrossRef]
14. Carroll, R.I.; Beynon, J.H. Rolling contact fatigue of white etching layer: Part 2. Numerical results. *Wear* **2007**, *262*, 1267–1273. [CrossRef]
15. Wang, L.; Pyzalla, A.; Stadlbauer, W.; Werner, E.A. Microstructure features on rolling surfaces of railway rails subjected to heavy loading. *Mater. Sci. Eng. A* **2003**, *359*, 31–43. [CrossRef]

16. Lojkowski, W.; Millman, Y.; Chugunova, S.I.; Goncharova, I.V.; Djahanbakhsh, M.; Bürkle, G.; Fecht, H.J. The mechanical properties of the nanocrystalline layer on the surface of railway tracks. *Mater. Sci. Eng. A* **2001**, *303*, 209–215. [CrossRef]
17. Wu, J.; Petrov, R.H.; Naeimi, M.; Li, Z.; Dollevoet, R.; Sietsma, J. Laboratory simulation of martensite formation of white etching layer in rail steel. *Int. J. Fatigue* **2016**, *91*, 11–20. [CrossRef]
18. Griffiths, B.J. White layer formations at machined surfaces and their relationship to white layer Formations at worn surfaces. *J. Tribol.* **1985**, *107*, 165. [CrossRef]
19. Umbrello, D.; Rotella, G. Experimental analysis of mechanisms related to white layer formation during hard turning of AISI 52100 bearing steel. *Mater. Sci. Technol.* **2012**, *28*, 205–212. [CrossRef]
20. Todaka, Y.; Umemoto, M.; Tsuchiya, K. Nanocrystallization in Carbon Steels by Various Severe Plastic Deformation Processes. In *Nanomaterials by Severe Plastic Deformation*; Wiley-VCH Verlag GmbH & Co. KGaA: Weinheim, Germany, 2004; pp. 505–510. ISBN 9783527602469.
21. Rauch, E.F.; Véron, M. Automated crystal orientation and phase mapping in TEM. *Mater. Charact.* **2014**, *98*, 1–9. [CrossRef]
22. Kobler, A.; Kashiwar, A.; Hahn, H.; Kübel, C. Combination of in situ straining and ACOM TEM: A novel method for analysis of plastic deformation of nanocrystalline metals. *Ultramicroscopy* **2013**, *128*, 68–81. [CrossRef] [PubMed]
23. Linz, M.; Cihak-Bayr, U.; Trausmuth, A.; Scheriau, S.; Künstner, D.; Badisch, E. EBSD study of early-damaging phenomena in wheel–rail model test. *Wear* **2015**, *342–343*, 13–21. [CrossRef]
24. Wu, J.; Petrov, R.H.; Naeimi, M.; Li, Z.; Sietsma, J. A Microstructural Study of Rolling Contact Fatigue in Rails. In Proceedings of the Second International Conference on Railway Technology: Research, Development and Maintenance, Ajaccio, France, 8–11 April 2014; Civil-Comp Press: Stirling, UK, 2014.
25. Hossain, R.; Pahlevani, F.; Witteveen, E.; Banerjee, A.; Joe, B.; Prusty, B.G.; Dippenaar, R.; Sahajwalla, V. Hybrid structure of white layer in high carbon steel–Formation mechanism and its properties. *Sci. Rep.* **2017**, *7*, 1–12. [CrossRef] [PubMed]
26. Kabekkodu, S. *ICDD (2014), PDF-4+ 2014 (Database)*; International Centre for Diffraction Data: Newtown Square, PA, USA, 2014.
27. NanoMEGAS. Available online: http://www.nanomegas.com/ (accessed on 20 February 2016).
28. Petrov, R.; Wu, J.; Sietsma, J. Microstructure of white etching layer of in-field loaded railway steel. In Proceedings of the International Scientific Congress: Machines, Technologies, Materials, Sofia, Bulgaria, 15–18 March 2017; Volume VII, pp. 505–508.
29. Zhou, D.S.; Shiflet, G.J. Ferrite: Cementite crystallography in pearlite. *Metall. Trans. A* **1992**, *23*, 1259–1269. [CrossRef]
30. Miller, M.K.; Beaven, P.A.; Brenner, S.S.; Smith, G.D.W. An Atom Probe Study of the Aging of Iron-Nickel-Carbon Martensite. *Metall. Mater. Trans. A* **1983**, *14*, 1021–1024.
31. Miller, M.K.; Beaven, P.A.; Smith, G.D.W. A Study of the early stages of tempering of iron-carbon martensites by atom probe field ion microscopy. *Metall. Trans. A* **1981**, *12*, 1197–1204. [CrossRef]
32. Krauss, G. Martensite in steel: Strength and structure. *Mater. Sci. Eng. A* **1999**, *273*, 40–57. [CrossRef]
33. Savran, V. Austenite Formation in C-Mn Steel. Ph.D. Thesis, Delft University of Technology, Delft, The Netherlands, February 2009.